

Fabrication and convergent X-ray nanobeam diffraction characterization of submicron-thickness SrTiO₃ crystalline sheets

J. A. Tilka, J. Park, K. C. Sampson, Z. Cai, and P. G. Evans

Citation: [APL Mater.](#) **4**, 126108 (2016); doi: 10.1063/1.4972528

View online: <http://dx.doi.org/10.1063/1.4972528>

View Table of Contents: <http://aip.scitation.org/toc/apm/4/12>

Published by the [American Institute of Physics](#)

Fabrication and convergent X-ray nanobeam diffraction characterization of submicron-thickness SrTiO₃ crystalline sheets

J. A. Tilka,¹ J. Park,¹ K. C. Sampson,¹ Z. Cai,² and P. G. Evans^{1,a}

¹Department of Materials Science and Engineering, University of Wisconsin-Madison, Madison, Wisconsin 53706, USA

²Advanced Photon Source, Argonne National Laboratory, Argonne, Illinois 60439, USA

(Received 4 October 2016; accepted 5 December 2016; published online 20 December 2016)

The creation of thin SrTiO₃ crystals from (001)-oriented SrTiO₃ bulk single crystals using focused ion beam milling techniques yields sheets with submicron thickness and arbitrary orientation within the (001) plane. Synchrotron x-ray nanodiffraction rocking curve widths of these SrTiO₃ sheets are less than 0.02°, less than a factor of two larger than bulk SrTiO₃, making these crystals suitable substrates for epitaxial thin film growth. The change in the rocking curve width is sufficiently small that we deduce that dislocations are not introduced into the SrTiO₃ sheets. Observed lattice distortions are consistent with a low concentration of point defects. © 2016 Author(s). All article content, except where otherwise noted, is licensed under a Creative Commons Attribution (CC BY) license (<http://creativecommons.org/licenses/by/4.0/>). [<http://dx.doi.org/10.1063/1.4972528>]

The creation of thin mechanically compliant complex oxide single crystals has the potential to enable new scientific and technological directions by allowing strain to be used in new ways to control functional properties ranging from electron transport to magnetism.¹ In existing demonstrations of this effect in covalent semiconductors, such as Si, the elastic compliance of nanoscale sheets can be used to create heterostructures that enable new strategies for the realization of quantum devices without defects resulting from plastic relaxation.^{2,3} A persistent challenge in advancing towards thin materials in perovskite complex oxides, however, is that lithographic processing of thin substrates can lead to low structural quality in terms of non-uniform thickness, roughness, buckling, or defect density.⁴⁻⁶ Alternative approaches based on chemical exfoliation of large-unit-cell oxide compounds can create ultrathin substrates but have a severely limited range of compositions and crystallographic orientations.⁷

In this Letter we report the creation and characterization of submicron-thickness SrTiO₃ (STO) sheets. The results demonstrate that focused ion beam (FIB) lithography techniques can be used to create a thin STO sheet with sufficiently low defect densities to allow subsequent use as substrates for thin film growth. Effects similar to what we report here will also be relevant to the large-area lithography techniques used in device applications. The submicron thickness scale of these sheets is particularly important because it enables elastic strain sharing over a critical range of imposed strains, 0.1%–1%, for which elastic distortions result in significant changes in the properties of complex oxides. Synchrotron x-ray nanodiffraction shows that the processing of these sheets does not introduce extended structural defects or large variations in lattice parameter and that the resulting materials have sufficient structural quality to serve as substrates for epitaxial growth.

Previous methods for the creation of thin oxide crystals have important limitations. Exfoliated sheets with thicknesses at the unit-cell scale can be fabricated using a colloidal suspension of perovskite sheets from a Dion-Jacobson phase.⁷ Exfoliation, however, yields a narrow range of thicknesses, on the order of 1–2 nm, has fixed (001) orientation set by the layering of the parent phase, and relatively small micron-scale crystals. A second method, epitaxial growth and lift-off, involves etching

^aElectronic mail: pgevans@wisc.edu

a sacrificial layer and transfer to a new substrate.^{8,9} Lift-off requires a specific combination of etchant chemistries and sacrificial layers and has so far been developed for only a few layer compositions and orientations.

Lithographic methods for the creation of nanostructures have employed physical patterning methods, including FIB lithography and reactive ion etching.¹⁰ The removal of material during patterning is accompanied by the creation of structural defects ranging from vacancies to extended defects.¹¹ Ion collisions lead to the removal of the milled material through a process that is not strongly dependent on oxide composition.¹¹ Ion-induced damage is a significant concern, however, in the use of FIB to create oxide nanostructures. The generation of defects during FIB is described using a collision cascade model, in which ions participate in a series of independent two-body collisions.¹² The ion-lattice collisions can displace atoms from lattice sites, creating vacancies and interstitials, which can coalesce to form dislocation.^{6,13} The resulting microstructure is described using a mosaic model and yields an increased angular width of x-ray reflections.¹⁴ In addition, vacancies in STO result in a well-known lattice expansion.¹⁵ At high ion doses there are sufficient atomic displacements to produce a transformation to an amorphous structure, either directly beneath or adjacent to the location of the ion beam. The transverse straggle of ions creates such an amorphous region with a depth of tens of nanometers and changes the chemistry and functional properties of material outside the region being milled.^{13,16,17}

Structural features introduced during milling, including mosaic blocks, strain, point defects, and curvature, result in an increase in the angular width of x-ray rocking curves.^{18,19} The intensity and width of the (002) Bragg reflection in Ga-ion-milled BiFeO₃ thin films, for example, are reduced and broadened as a result of the electric fields of surface charges and defects.¹⁹ Bragg reflections of STO thin films can be broadened by misfit dislocations resulting from epitaxial growth and a similar effect can be expected from ion milling.¹⁸

The substrates for this study were (001)-oriented STO single crystals (Crystec, Inc.). Ion milling was performed with a Ga⁺ ion beam at an ion kinetic energy of 30 keV. A protective amorphous C layer with a thickness of 1 μm was deposited before milling using ion-beam-activated local chemical vapor deposition to protect a 1 $\mu\text{m} \times 14 \mu\text{m}$ area. The C deposition process was conducted by introducing a hydrocarbon gas precursor while a 50 pA ion beam was rastered through the deposition area. The 1 μm thickness of the protective layer is larger than the 10–100 nm stopping depth of the ions.¹²

The ion milling was conducted in three steps of decreasing beam current, using a procedure based on the lift-out method of transmission electron microscopy sample preparation.^{11,20} An initial coarse milling step at a relatively high current of 14 nA was used to create a trench with a depth of 10 μm surrounding the region in which the sheet was fabricated. The trench was designed to allow subsequent characterization using x-ray nanodiffraction. Milling at an intermediate current of 4 nA then removed STO to within approximately 500 nm of the final sheet. A low-current fine milling step was then conducted at 300 pA. Scanning electron microscopy (SEM) images of an STO sheet with a [110] surface normal and a thickness of 500 nm are shown in Figs. 1(a) and 1(b).

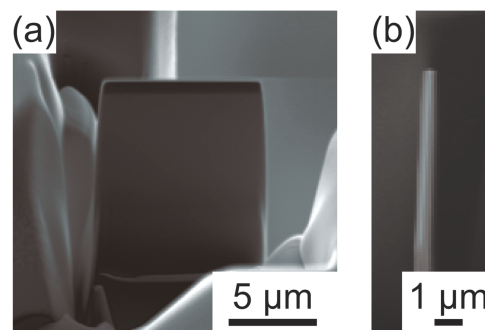


FIG. 1. SEM image of (a) large (110) face and (b) top edge of a 500-nm-thick STO sheet produced by FIB milling. The dimensions of the face are $9.5 \mu\text{m} \times 10.2 \mu\text{m}$. The darker region on the top is the protective C cap.

Sheets with different thermal histories were created in order to evaluate the effects of thermal annealing in air on the STO sheets and on the near-surface regions of the bulk substrates. The annealing step was conducted at 1000 °C for 50 h, which was reached with heating and cooling rates of 20 °C/min. The annealing temperature was sufficiently high to recrystallize surface amorphous layers with thicknesses on the order of 10 nm that result from transverse straggle of Ga ions.¹¹ Previous studies of the recrystallization of amorphous STO, created either through ion bombardment or sputter deposition, indicate that recrystallization occurs on this time scale.^{21,22} Samples were sputter-coated with a 100 nm carbon layer to reduce charging during x-ray exposure, which can lead to chemical and structural degradation in insulators.²³

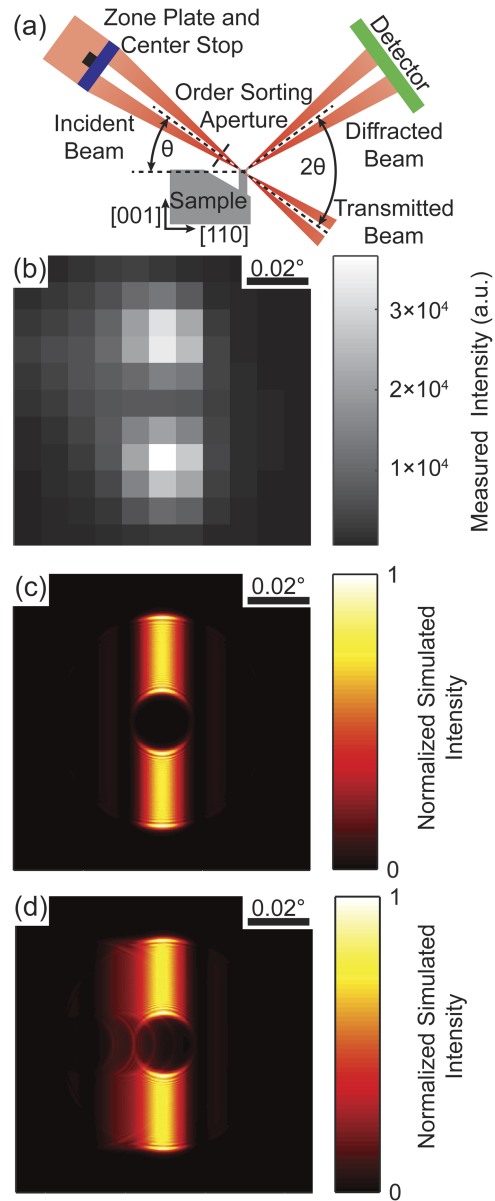


FIG. 2. (a) Schematic of the synchrotron x-ray nanodiffraction experiment. (b) Experimental diffraction pattern of the (002) Bragg reflection of a (110)-oriented annealed STO sheet. (c) Simulated (002) diffraction pattern using the same focusing optics as in the experiment and an ideal 500 nm thick STO sample. (d) Five incoherently summed mosaic blocks of STO with orientations differing in θ over a range of 0.013° . The off-center blocks each have one eighth the intensity of the block in the center of the image.

X-ray nanobeam diffraction studies were conducted using zone-plate x-ray focusing optics at station 2ID-D of the Advanced Photon Source at Argonne National Laboratory. The diffraction experiment was conducted in a transmission geometry, as shown in Fig. 2(a), in order to avoid illuminating the STO substrate. The x-ray photon energy was $E = 10.1$ keV, selected with a double-bounce Si (111) monochromator. The zone plate had diameter $D_{zp} = 160$ μm , outermost zone width 100 nm, zone thickness 1.6 μm , and focal length $L_f = 130$ mm at 10.1 keV. The center stop and order-sorting aperture consisted of a 60 μm -thick Au cylinder with a 40 μm diameter and a 20 μm -diameter hole in a Pt disk, respectively. The x-ray focal spot has a large angular convergence, $D_{zp}/L_f = 0.07^\circ$, leading to complex diffraction patterns. The focused beam had a full-width-at-half-maximum (FWHM) diameter of approximately 200 nm at the sample. Diffracted x-rays were detected with a charge-coupled device with 80 μm pixels (Mar 165, Mar, Inc.).

Experimental diffraction patterns from milled and annealed (110)-oriented 500-nm-thick STO sheets are shown in Fig. 2(b). The incident angle of the center of the focused beam for Fig. 2(b) was $\theta = 18.322^\circ$, which corresponds to the STO (002) Bragg reflection. X-ray rocking curves were acquired by scanning the x-ray incident angle, θ , through a total range of 0.1° . Interpreting rocking curves acquired with a nanobeam is challenging because the incoming x-ray beam is not defined by a single wavevector, but a range of wavevectors corresponding to the angular divergence of the focused x-ray beam.

The diffraction experiment was simulated using wave-optics methods that faithfully reproduce the angular and spatial beam distribution at the focal spot, followed by a simulation of kinematic diffraction by the sample, and propagation to the detector.^{24,25} A simulated diffraction pattern with focusing optics and sample orientation matching the experiment is shown in Fig. 2(c). The region of high intensity in Fig. 2(c) vertically spans the angle subtended by the zone plate and has a horizontal width inversely proportional to the height of the illuminated region of the sample. The dark circle at the center of the simulated diffraction pattern in Fig. 2(c) corresponds to the projection of the shadow of the center stop onto the x-ray detector.

An additional complication arises because mosaic blocks with orientations differing from the nominal Bragg condition by an angle less than half of the beam divergence also satisfy the Bragg condition for some part of the convergent incident beam. A defective sample was considered by simulating multiple crystals with angular offsets. The scattering from each mosaic block was summed incoherently to simulate diffraction patterns from mosaic crystals. Fig. 2(d) shows a simulated diffraction pattern of a distribution of five mosaic blocks with identical lattice parameters misoriented equally over a range of 0.013° in θ . The relative intensity and mutual orientation of the misoriented blocks were chosen in order to match the experimental result in Fig. 2(a). Note that the difference in the orientation of the blocks allows them to be distinguished in the diffraction pattern.

Diffraction patterns for an experimental rocking curve of an unprocessed STO crystal are shown in Fig. 3(a). Fig. 3(a) shows diffraction patterns of the (002) Bragg reflection acquired at different sample orientations. Fig. 3(a) exhibits a vertical region of high diffracted intensity that moves across the detector. The shadow of the center stop appears at the center of the image at $\theta = 18.322^\circ$. The diffraction pattern has high intensity at all angles within a range equal to the angular divergence of the incident focused x-ray nanobeam.

The mosaic distribution within a conventional rocking curve scan is evaluated by measuring the angular width of the integrated diffracted x-ray intensity as a function of the sample orientation.²⁶ With the convergent focused x-ray nanobeam, however, the angular width of the total intensity is set by the beam divergence rather than by the mosaic width. Fig. 3(b) shows the integrated intensity as a function of the sample orientation, exhibiting a full-width-at-tenth-maximum of 0.073° , matching the angular width of the incident beam, 0.070° .

Examining the dependence of the intensity within small areas of the diffraction patterns as a function of sample orientation allows far more precise study of the mosaicity of the sample than the total integrated intensity. The intensity integrated in a smaller region of the detector, as shown in Fig. 3(c), exhibits features much narrower than the angular width of the total integrated intensity. When a narrow range of the detector is integrated, the x-ray rocking curve has an angular width set by the angular width of the detector pixel, in this case 0.01° , rather than by the entire focused beam. We

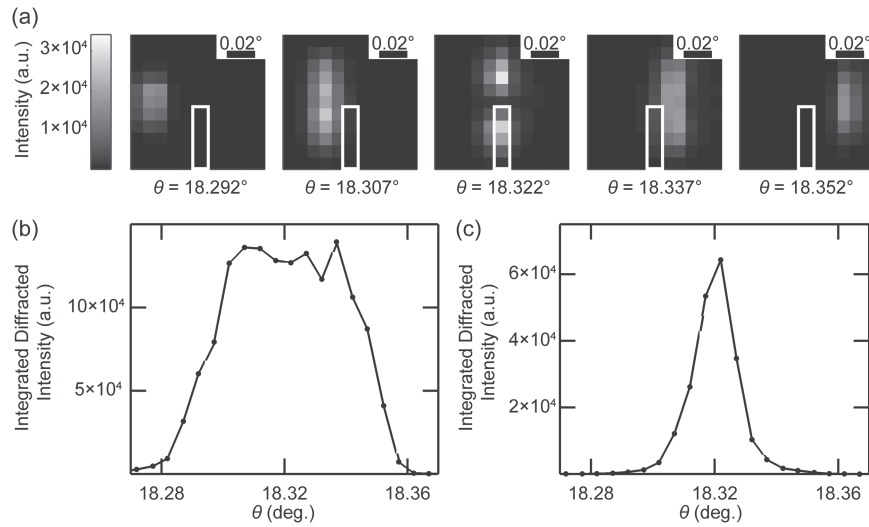


FIG. 3. (a) Diffraction patterns of the (002) Bragg reflection from bulk unprocessed STO acquired with different sample orientations ranging from $\theta = 18.292^\circ$ to $\theta = 18.352^\circ$. The region of high x-ray intensity moves from left to right as θ increases. The shadow of the center stop is apparent at $\theta = 18.322^\circ$. (b) Integrated intensity as a function of angle for the diffraction patterns shown in (a). The intensity of the rocking curve is approximately constant over an angular range equal to the zone plate divergence because part of the divergent beam meets the Bragg condition for all angles in this range. (c) Narrow rocking curves produced by integrating within the region of interest indicated by the white box in (a).

have neglected other sources of broadening such as the finite energy bandwidth of the experiment. The intensity peak in Fig. 3(c) has a FWHM of 0.011° , matching this expectation.

X-ray rocking curve measurements were used to examine the degree of homogeneity in the STO sheets and to evaluate the structural effect of each processing step. Structural studies using the method shown in Fig. 3(c) were repeated at multiple locations for milled and unmilled STO sheets and annealed STO substrates. Histograms of the angular widths of the diffracted intensity are shown in Fig. 4(a). The angular widths increase from 0.010° to 0.014° upon annealing. A possible origin of the increased mosaic width after annealing is a change in the oxygen vacancy concentration in the surface region of STO due the difference between the annealing conditions and the bulk STO growth conditions. At this energy and incident angle, the x-rays penetrate to a depth of approximately $10\ \mu\text{m}$ in bulk STO. A variation in the lattice parameter over the thickness probed by the x-rays imposes a strain gradient and increases the rocking curve width.

The FIB patterning and annealing processes lead to slight increases in the rocking curve angular width in comparison with bulk STO. Fig. 4(b) shows a histogram of the narrow-region rocking curve widths taken from a series of locations across the (110)-oriented STO sheets with a thickness of 500 nm. The x-ray rocking curves were acquired from regions of the samples that were separated by distances of 200 nm. The most frequently observed width in both annealed and unannealed sheets is 0.016° . The process of patterning the STO sheets thus resulted in an increase of rocking curve width from 0.01° to 0.016° .

There are several possible origins of the slight increase in width arising from the patterning and annealing of the STO samples. We first consider the possibility that the increase results from the introduction of dislocations into the STO sheet during the patterning. An upper limit of the dislocation density in the sheet can be determined by assuming that each dislocation creates a mosaic block. The dislocation density required to produce the observed width can be found using $D_{dis} = (\Delta\beta)^2/9b^2$, where D_{dis} is the dislocation density, $\Delta\beta$ is the rocking curve width, and b is the Burgers vector.¹⁸ The most common Burgers vector observed in TEM studies of STO is $1/2\langle 110 \rangle$.²⁷ The dislocation density corresponding to an angular width of a 0.016° -wide rocking curve in STO is thus $10^7\ \text{cm}^{-2}$. This density is sufficiently small that we cannot expect even one dislocation within the area defined by the beam width and the sample thickness. This density of dislocations is thus sufficiently low that we cannot attribute the small increase in mosaic width to the introduction of dislocations in the sheet during milling and annealing.

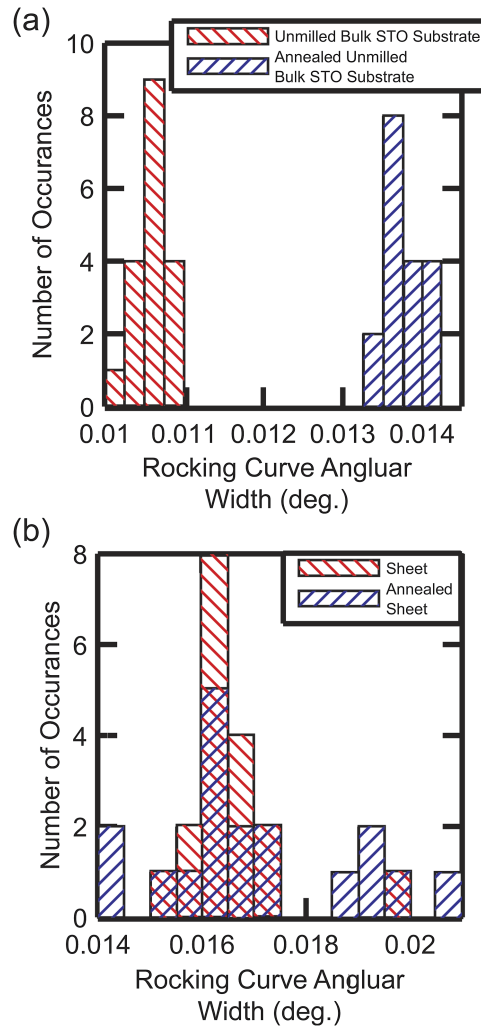


FIG. 4. (a) Histograms of rocking curve widths of bulk STO before and after annealing. (b) Histograms of rocking curve widths of STO sheets. The most frequent width in both cases is 0.016°.

A second possibility is that the angular width of the STO reflections arises from the overall curvature of the 500-nm-thick STO sheet. The curvature was separately measured by examining the systematic shift in the Bragg angle as a function of the position of the x-ray beam as it was scanned along the height of a single milled and unannealed sheet through points spaced 200 nm apart. The radius of curvature measured in this way was $R = 7$ mm. The effective difference in orientation across the illuminated region of the sheet is $\Delta z/R$, where Δz is the illuminated height given by $\Delta z = (t + s\sqrt{2}) \tan(\theta) + t/\cos(\theta)$ and t and s are the focal spot size and sheet thickness, respectively. The expected angular width due to the curvature of the sheet is thus 0.005°, which is only a factor of two less than the difference in quadrature between the angular width of the bulk unprocessed STO and the unannealed STO sheets.

The creation of point defects such as oxygen vacancies can be studied by evaluating the change in the average lattice parameter of the sheets. The lattice expansion, Fig. 5, was calculated using the 2θ angle (defined as in Fig. 2(a)) with the peak intensity in the rocking curve scans. The lattice expansion after milling was 0.06%, referred to the bulk STO lattice parameter. The subsequent annealing step reduces the expansion to 0.03%. An oxygen vacancy concentration of approximately 0.09% of the total number of oxygen lattice sites would result in the observed lattice parameter.¹⁵ We thus conclude that the oxygen vacancy concentration is less than 0.1% after the FIB process. A gradient of lattice parameters resulting from an inhomogeneous distribution of vacancies would also alter the rocking

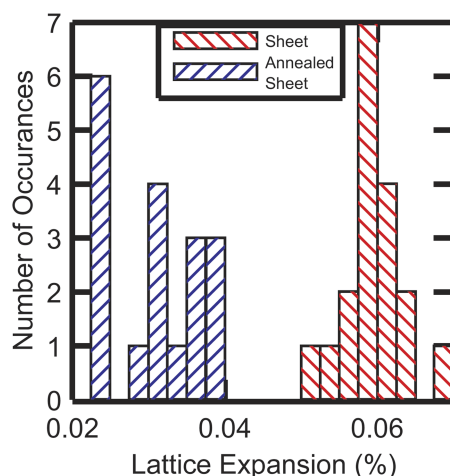


FIG. 5. Histograms of the lattice expansion in STO sheets acquired in the same locations as Fig. 4(b).

curve widths. We hypothesize that the process of annealing in air reduces the concentration of oxygen vacancies and thus accounts for the reduction in lattice expansion after annealing.

We have shown here that focused ion beam methods can be used to create oxide crystals that we expect are thin enough to be elastically compliant with arbitrary orientation and low defect density. The creation of thin oxide sheets by FIB, and in principle by other lithographic patterning techniques, provides a promising route towards the future use of strain engineering in complex oxide systems. X-ray nanodiffraction using tightly focused beams indicates that the increase in the rocking curve width is at most a factor of two, small enough that mosaic widths fall within a range typically used for epitaxial growth.²⁸

The development of the x-ray nanobeam analysis methods employed in this work was supported by the U.S. DOE, Basic Energy Sciences, Materials Sciences and Engineering, Contract No. DE-FG02-04ER46147. J.A.T. acknowledges support from the National Science Foundation Graduate Research Fellowship Program, Grant No. DGE-1256259 and from NSF Grant No. DMR-1106050. Use of the Advanced Photon Source was supported by the U.S. Department of Energy, Office of Science, Office of Basic Energy Sciences, under Contract No. DE-AC02-06CH11357. This research used shared facilities supported by the University of Wisconsin Materials Research Science and Engineering Center, NSF Grant No. DMR-1121288. The authors would like to thank Eli Mueller for carefully reviewing the simulation.

- ¹ D. G. Schlom, L.-Q. Chen, C. J. Fennie, V. Gopalan, D. A. Muller, X. Pan, R. Ramesh, and R. Uecker, *MRS Bull.* **39**, 118 (2014).
- ² M. M. Roberts, L. J. Klein, D. E. Savage, K. A. Slinker, M. Friesen, G. Celler, M. A. Eriksson, and M. G. Lagally, *Nat. Mater.* **5**, 388 (2006).
- ³ P. M. Mooney, G. M. Cohen, J. O. Chu, and C. E. Murray, *Appl. Phys. Lett.* **84**, 1093 (2004).
- ⁴ D. M. Paskiewicz, D. E. Savage, M. V. Holt, P. G. Evans, and M. G. Lagally, *Sci. Rep.* **4**, 4218 (2014).
- ⁵ G. Gopalakrishnan, D. A. Czaplewski, K. M. McElhinny, M. V. Holt, J. C. Silva-Martínez, and P. G. Evans, *Appl. Phys. Lett.* **102**, 033113 (2013).
- ⁶ C. R. Hutchinson, R. E. Hackenberg, and G. J. Shiflet, *Ultramicroscopy* **94**, 37 (2003).
- ⁷ B. W. Li, M. Osada, T. C. Ozawa, Y. Ebina, K. Akatsuka, R. Ma, H. Funakubo, and T. Sasaki, *ACS Nano* **4**, 6673 (2010).
- ⁸ D. Paskiewicz, R. Sichel-Tissot, E. Karapetrova, L. Stan, and D. D. Fong, *Nano Lett.* **16**, 534 (2016).
- ⁹ D. Lu, D. J. Baek, S. S. Hong, L. F. Kourkoutis, Y. Hikita, and H. Y. Hwang, *Nat. Mater.* **15**, 1255 (2016).
- ¹⁰ R. Maaß, D. Grolimund, S. Van Petegem, M. Willmann, M. Jensen, H. Van Swygenhoven, T. Lehnert, M. A. M. Gijs, C. A. Volkert, E. T. Lilleodden, and R. Schwaiger, *Appl. Phys. Lett.* **89**, 151905 (2006).
- ¹¹ J. Mayer, L. A. Giannuzzi, T. Kamino, and J. Michael, *MRS Bull.* **32**, 400 (2007).
- ¹² C. A. Volkert and A. M. Minor, *MRS Bull.* **32**, 389 (2007).
- ¹³ S. Rubanov and P. R. Munroe, *J. Microsc.* **214**, 213 (2004).
- ¹⁴ P. Gay, P. B. Hirsch, and A. Kelly, *Acta Metall.* **1**, 315 (1953).
- ¹⁵ H. L. Cai, X. S. Wu, and J. Gao, *Chem. Phys. Lett.* **467**, 313 (2009).
- ¹⁶ D. Kiener, C. Motz, M. Rester, M. Jenko, and G. Dehm, *Mater. Sci. Eng. A* **459**, 262 (2007).
- ¹⁷ A. Stanishvsky, B. Nagaraj, J. Melngailis, R. Ramesh, L. Khriachtchev, and E. McDaniel, *J. Appl. Phys.* **92**, 3275 (2002).

- ¹⁸ Z. Y. Zhai, X. S. Wu, H. L. Cai, X. M. Lu, J. H. Hao, J. Gao, W. S. Tan, Q. J. Jia, H. H. Wang, and Y. Z. Wang, *J. Phys. D: Appl. Phys.* **42**, 105307 (2009).
- ¹⁹ W. Siemons, C. Beekman, J. D. Fowlkes, N. Balke, J. Z. Tischler, R. Xu, W. Liu, C. M. Gonzales, J. D. Budai, and H. M. Christen, *APL Mater.* **2**, 22109 (2014).
- ²⁰ T. Yaguchi, T. Kamino, T. Ishitani, and R. Urao, *Microsc. Microanal.* **5**, 365 (1999).
- ²¹ C. W. White, L. A. Boatner, P. S. Sklad, C. J. McHargue, J. Rankin, G. C. Farlow, and M. J. Aziz, *Nucl. Instrum. Methods Phys. Res., Sect. B* **32**, 11 (1988).
- ²² F. Wang, M. Badaye, Y. Yoshida, and T. Morishita, *Nucl. Instrum. Methods Phys. Res., Sect. B* **118**, 547 (1996).
- ²³ L. Gregoratti, T. O. Montes, A. Locatelli, and M. Kiskinova, *J. Electron Spectrosc. Relat. Phenom.* **170**, 13 (2009).
- ²⁴ A. Ying, B. Osting, I. C. Noyan, C. E. Murray, M. Holt, and J. Maser, *J. Appl. Crystallogr.* **43**, 587 (2010).
- ²⁵ J. A. Tilka, J. Park, Y. Ahn, A. Pateras, K. C. Sampson, D. E. Savage, J. R. Prance, C. B. Simmons, S. N. Coppersmith, M. A. Eriksson, M. G. Lagally, M. V. Holt, and P. G. Evans, *J. Appl. Phys.* **120**, 15304 (2016).
- ²⁶ T. B. U. Pietsch and V. Holy, *High-Resolution X-Ray Scattering* (Springer, New York, 2004).
- ²⁷ J. Yamanaka, *Mater. Trans.* **42**, 1131 (2001).
- ²⁸ M. D. Biegalski, D. D. Fong, J. A. Eastman, P. H. Fuoss, S. K. Streiffer, T. Heeg, J. Schubert, W. Tian, C. T. Nelson, X. Q. Pan, M. E. Hawley, M. Bernhagen, P. Reiche, R. Uecker, S. Trolier-Mckinstry, and D. G. Schlom, *J. Appl. Phys.* **104**, 114109 (2008).